# The role of the field-effect emission in Trichel pulse development in air at atmospheric pressure

View the article online for updates and enhancements.
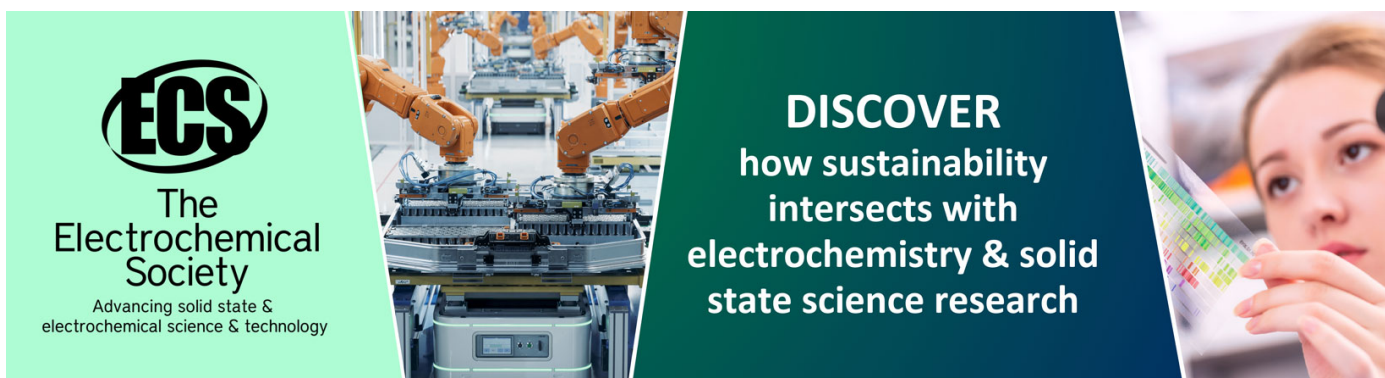
# The role of the field-effect emission in Trichel pulse development in air at atmospheric pressure

**T Reess and J Paillol**

Laboratoire de Génie Electrique, Université de Pau, 64000 Pau, France

**Abstract.** Several theories have been proposed to explain the current pulse of Trichel, at low pressure, in accordance with experimental results. Nevertheless, these theories failed to explain the very fast rise time (a few nanoseconds) observed at high pressure. The aim of this study is to propose a numerical simulation of the Trichel pulse which explains the typical current shape observed in air at atmospheric pressure in terms of field-effect emission. This theory explains the principal mechanisms responsible for the formation of Trichel pulses and takes into account the cathode material and its surface state. The effects of the field magnification factor on the pulse shape resulting from cathode microprotrusions are discussed. In the same way, the value of the discharge channel's radius is also discussed and compared with the experimental measurements.

## 1. Introduction

When a sufficiently high negative voltage is applied to a point–plane gap in an electronegative gas such as air, regular corona current pulses are observed. These regular current pulses, called Trichel pulses, were first studied by Trichel (1938).

A model of the pulse formation was developed by Loeb (1965). The author attempted to explain the pulses as follows: electrons, ejected from the cathode surface, create an avalanche near the cathode, causing an exponential or even more rapid rise of the current. The positive ions thus created at some distance from the cathode remain practically stationary and lead to a strong formation of positive space charge which rapidly increases the initial ionization. The electrons proceed out into the gap beyond the positive space charge. They are transformed into negative ions by attachment and thus build up a slow-moving cloud of negative-ion space charge. The positive-ion movement shortens the effective high field, although it increases its strength. This action, together with the influence of the negative-ion space charge, reduces the effective field near the cathode and leads to the discharge being quenched. Then the discharge remains extinguished until the negative space charge has dissipated.

Loeb's predictions were confirmed by Morrow (1985a, b), who presented theoretical calculations accounting for the development of Trichel pulses in oxygen at low pressure (6.67 kPa). Morrow's theory explains the formation of current pulses in terms of photoelectric-effect emission and secondary ion processes at the cathode.

Nevertheless, Loeb (1965) and Cernak and Hosokawa (1991, 1992) showed that, at high pressure (above 30 kPa), the fast rise time of the current pulse cannot be explained in terms of the photoelectric effect alone. Indeed, in air at atmospheric pressure, this rise time has been experimentally measured to be of the order of $10^{-9}$ s (Lama and Gallo 1974, Torsethaugen and Sigmond 1973). This characteristic time is shorter than the one of $60 \times 10^{-9}$ s corresponding to the life time of the excited states of nitrogen and oxygen molecules in air at atmospheric pressure (Laurence *et al* 1968). Consequently, these excitation processes, which lead to the release of photoelectrons at the cathode, are neglected. Reess *et al* (1995a, b) measured the 100 MHz repetition rate of Trichel pulses under a bi-exponential voltage impulse in a large air gap.

This paper presents a numerical simulation (Reess *et al* 1997) of the Trichel current pulse in air at atmospheric pressure. The continuity equations of electron, positive-ion and negative-ion densities are solved numerically on a nonuniform mesh using the explicit–implicit flux-corrected transport (FCT) algorithm. Those equations are coupled to Poisson's equation via the charge density. This simulation takes into account the field-effect emission from the cathode and explains the fast rise time of the current pulse which is characteristic at high pressure.

## 2. The theory

### 2.1. Basic equations

**2.1.1. Continuity equations.** The theory is based on a classic one-dimensional hydrodynamic model in which the continuity equations for electrons, positive ions

and negative ions are used only to describe the axial development of the discharge:

$$\frac{\partial}{\partial t} N_e + \frac{\partial}{\partial x} N_e W_e = (\alpha - \eta) W_e N_e - \beta N_e N_p$$

$$\frac{\partial}{\partial t} N_p + \frac{\partial}{\partial x} N_p W_p = \alpha W_e N_e - \beta N_e N_p - \beta N_n N_p$$

$$\frac{\partial}{\partial t} N_n + \frac{\partial}{\partial x} N_n W_n = \eta W_e N_e - \beta N_n N_p \qquad (1)$$

where $t$ is time, $x$ is the distance from the cathode, $N_e$, $N_p$ and $N_n$ are the electron, positive-ion and negative-ion densities, respectively, and $W_e$, $W_p$ and $W_n$ are electron, positive-ion and negative-ion drift velocities, respectively. The material functions $\alpha$, $\beta$ and $\eta$ are, respectively the ionization, recombination and attachment coefficients. They are determined entirely by the local reduced electric field $E/N$, where $E$ is the electric field and $N$ is the neutral gas density. Diffusion is not included, since its inclusion has a negligible effect on the results but increases the computing time (Bayle 1975, Morrow 1985a).

**2.1.2. The electric field.** In order to determine the spatio-temporal development of a discharge, it is necessary to calculate the total electric field. The axial geometrical component $E_G(x)$ of the electric field is calculated with a hyperboloid approximation given by (Boutteau 1967)

$$E_G(x) = \frac{2U_0}{R \ln\left(\frac{4D}{R}\right)} \frac{1}{1 - \frac{x}{D}\left(1 - \frac{2D}{R}\right) - \left(\frac{x}{D}\right)^2 \frac{D}{R}} \qquad (2)$$

where $U_0$ is the applied voltage, $R$ is the cathode radius. The gap extends from $x = 0$ (at the cathode) to $x = D$ (at the anode)

Davies and Evans (1967) described a method called the 'disc method' which gives the axial distribution of the space-charge field with a high degree of accuracy. In this method, the discharge is divided into discs by planes perpendicular to the axis and the field on the axis is found by computing the contribution of each disc of charge, making the appropriate allowance for the image charges in the electrodes. In such a model the axial component of the electric field $E_c(x)$ at point $x$ is given by

$$E_c(x) = \frac{1}{2e_0}\left[\int_{-x}^{0} \rho(x + x')\left(-1 - \frac{x'}{(x'^2 + r^2)^{1/2}}\right) dx' \right.$$
$$\left. + \int_{0}^{D-x} \rho(x + x')\left(1 - \frac{x'}{(x'^2 + r^2)^{1/2}}\right) dx'\right] \qquad (3)$$

where $\rho(x)$ is the net charge density at $x$ and $r$ is the cylinder's radius.

Thus, the axial total electric field $E(x)$ at point $x$ is calculated by

$$E(x) = E_G(x) + E_c(x). \qquad (4)$$

**2.1.3. Boundary conditions.** At absorbing boundaries, the particle densities are finite and determined by the flux from the body of the discharge (Morrow 1985a). All continuity equations are first order and require one

boundary condition each. We set $N_n(x = 0) = 0$ and $N_p(x = D) = 0$. At the cathode, we set

$$N_e(x = 0) = N_e(\gamma) + N_{e(Fowler)} \qquad (5)$$

where $N_{e(\gamma)}$ is the density of secondary electrons released by ion impacts and $N_{e(Fowler)}$ is the density of electrons emitted by the field effect. $N_{e(\gamma)}$ is given by

$$N_{e(\gamma)}(x = 0) = \gamma \frac{N_p(0, t)|W_p(0, t)|}{|W_e(0, t)|} \qquad (6)$$

where $\gamma = 10^{-2}$ is the ion-secondary-emission coefficient. $N_{e(Fowler)}$ is calculated using the Fowler–Nordheim (1928) relationship:

$$j = B_1 \frac{E^2}{\Phi t^2(y)} \exp\left(-B_2 v(y)\frac{\Phi^{3/2}}{E}\right) \qquad (7)$$

with $y = 3.79 \times 10^{-5}\sqrt{E/\Phi}$, where $j$ is the current density (A m$^{-2}$), $E$ is the electric field on the cathode surface (V m$^{-1}$), $\Phi$ is the metal workfunction of the cathode material (electron-volts), $t(y)$ and $v(y)$ are special functions of the $y$ variable (Fowler and Nordheim 1928), $B_1 = 1.54 \times 10^{-6}$ A eV V$^{-2}$ and $B_2 = 6.83 \times 10^9$ V m$^{-1}$ eV$^{3/2}$.

Several experiments (Rohrbach 1971) have shown that the use of a strong electric field ($E \simeq 10^7$–$10^8$ V m$^{-1}$) leads to electron emission by the field effect from microscopic protrusions ($\simeq 1$ $\mu$m high) which are confined on the cathode surface. On the top of these microscopic tips, the electric field $E$ can be at least 10–100 times higher than the field on the cathode surface $E_0$. In order to take into account the real values of the electric field on the cathode surface, a field magnification factor $\beta^*$ is used:

$$E = \beta^* E_0. \qquad (8)$$

Consequently, two coefficients are used to characterize the field-effect emission from the cathode: its metal workfunction $\Phi$ and its surface state $\beta^*$.

**2.1.4. The current.** The current $I$ in the external circuit due to the motion of electrons and ions is calculated using Sato's equation (Sato 1980):

$$I = \frac{\pi r^2 e}{U_0} \int_0^d (N_p W_p - N_n W_n - N_e W_e) E \, dx \qquad (9)$$

where $e$ is the electron charge.

**2.2. Numerical techniques**

The system of equations (1) is solved using the classic flux-corrected transport (FCT) method which was originally developed by Borris and Book (1976). Since then, this technique has been used extensively by Morrow and Cram (1983, 1985), Morrow (1985a, 1987), Steinle and Morrow (1989) and Wang and Kunhardt (1990) in the simulation of discharges. The numerical FCT techniques used are identical to those proposed by Steinle and Morrow (1989). Therefore they will not be described here in detail.

Nevertheless, the main structure of the implicit–explicit FCT algorithm is presented.

Two interleaved mesh spacings are defined:

$$\delta x_{j+1/2} = x_{j+1} - x_j$$

$$\delta x_j = \tfrac{1}{2}(\delta x_{j+1/2} + \delta x_{j-1/2}).$$

We define the Courant number $c_{j+1/2}$ as

$$c_{j+1/2} = \delta t \frac{W_{j+1/2}}{\delta x_{j+1/2}}$$

where $\delta t$ is the time step and $W_{j+1/2}$ is the drift velocity between mesh points $j$ and $j + 1$. The implicit–explicit flux-corrected transport algorithm is used to represent the drift term of the typical equation accurately:

$$\frac{\partial}{\partial t}\rho + \frac{\partial}{\partial x}(\rho W) = 0 \qquad (10)$$

where $\rho$ is the particle density. We solve this equation on a variable nonuniform mesh defined along the axis of symmetry of the electrode system as the set

$$x_i = x_{i-1} + \delta x_i \;\; (i = 1, 2, \ldots, 145)$$

with the cathode surface at $x_0 = 0$ cm and the anode surface at $x_{145} = 1.6$ cm. A very fine-meshed resolution of $\delta x_i = 10^{-4}$ cm is required in the cathode region $0 < x_i < 0.005$ cm (50 nodes):

$\delta x_i = 2 \times 10^{-4}$ cm for $0.005 < x_i < 0.01$ cm (25 nodes)

$\delta x_i = 10 \times 10^{-4}$ cm for $0.01 < x_i < 0.02$ cm (ten nodes).

On the anode region ($0.02 < x_i < 1.6$ cm) the mesh is steadly expanded using 60 nodes. Consequently, 60% of the 145 nodes are used to describe only 1.25% of the gap length.

We follow Zalesak's (1979) approach and compute both a low-order solution and a high-order solution. For the low-order scheme we use upwind differences, a simple explicit technique which guarantees non-negative results with minimal numerical diffusion:

$$\delta x_j \tilde{\rho}_j = \delta x_j \rho_j^n - \delta x_{j+1/2} c_{j+1/2} \rho_j^n + \delta x_{j-1/2} c_{j-1/2} \rho_{j-1}^n$$

where $\tilde{\rho}_j$ is the low-order solution at point $j$ and step time $n + 1$ and $\rho_j^n$ is the density at time $n$. For the high-order scheme a fourth-order space- and time-centred method is used:

$$\delta x_j \bar{\rho}_j + \frac{1}{4}[\delta x_{j+1/2} c_{j+1/2}(\bar{\rho}_{j+1} + \bar{\rho}_j)$$
$$- \delta x_{j-1/2} c_{j-1/2}(\bar{\rho}_j + \bar{\rho}_{j-1})]$$
$$+ \delta x_{j+1/2}\frac{2 + c_{j+1/2}^2}{12}(\bar{\rho}_{j+1} - \bar{\rho}_j)$$
$$- \delta x_{j-1/2}\frac{2 + c_{j-1/2}^2}{12}(\bar{\rho}_j - \bar{\rho}_{j-1})$$
$$= \delta x_j \rho_j - \frac{1}{4}[\delta x_{j+1/2} c_{j+1/2}(\rho_{j+1} + \rho_j)$$
$$- \delta x_{j-1/2} c_{j-1/2}(\rho_j + \rho_{j-1})]$$
$$+ \delta x_{j+1/2}\frac{2 + c_{j+1/2}^2}{12}(\rho_{j+1} - \rho_j)$$

$$- \delta x_{j-1/2}\frac{2 + c_{j-1/2}^2}{12}(\rho_j - \rho_{j-1})$$

where $\bar{\rho}_j$ is the high-order solution to the implicit scheme at point $j$ and time level $n + 1$.

Then, we can compute the high- and low-order fluxes, respectively $\Phi_{j+1/2}^{*I}$ and $\Phi_{j+1/2}^{*E}$, which represent the fluxes of particles across a cell boundary due to the application of the high- and low-order schemes:

$$\Phi_{j+1/2}^{*E} = \delta x_{j+1/2}\rho_j$$
$$\Phi_{j+1/2}^{*I} = \delta x_{j+1/2}\left(\frac{2 + c_{j+1/2}^2}{12}(\bar{\rho}_{j+1} - \bar{\rho}_j - \rho_{j+1} + \rho_j)\right.$$
$$\left. + \frac{c_{j+1/2}}{4}(\bar{\rho}_{j+1} + \bar{\rho}_j + \rho_{j+1} + \rho_j)\right).$$

Hence, the total anti-diffusive flux required to remove the numerical diffusion is

$$\Phi_{J+1/2}^* = \Phi_{j+1/2}^{*E} + \Phi_{j+1/2}^{*I}.$$

Nevertheless, the anti-diffusive flux application must be limited in order not to generate new spurious maxima and minima. Thus, we use the flux limiter of Boris and Book (1976) and compute a new complete solution at point $j$ and time level $n + 1$:

$$\rho_j^{n+1} = \tilde{\rho}_j + \frac{1}{\delta x_j}(\bar{\Phi}_{j-1/2}^* - \bar{\Phi}_{j+1/2}^*).$$

This implicit–explicit FCT algorithm gives non-negative and accurate results for Courant numbers $c < 1$.

To compute the densities' behaviour with time, only due to the source term, we use the second-order Runge–Kutta technique (Morrow 1987). These complete intermediate solutions half a time step ahead are then used to compute a full time step from the present time level to the advanced time level using the FCT algorithm.

## 3. Results

The experimental measured Trichel current pulses in air at atmospheric pressure (Torsethaugen and Sigmond 1973) are presented in figure 1 (in a system with a tip of 0.074 mm radius and a 16 mm gap). The applied voltage is $-4.25$ kV. Two kinds of cathode materials were used. The main features of the impulse shape, obtained with the Mo and Au cathode, are the rise time shorter than 3 ns, its peak value of 4 mA and a step on the leading edge.

The computed current obtained in the same experimental system is shown in figure 2. For the calculation, we used a value of $\Phi = 4.5$ eV corresponding to the mean values of the workfunctions of Mo and Au. The discharge was considered to be a cylinder of 0.5 mm radius and the field magnification factor $\beta^*$ was put equal to 120. The validity of those two values will be discussed in section 4. The main features of the theoretical current pulse are in accordance with the experimental results: a rise time of about 3 ns, a peak value of about 4 mA and a step on the leading edge.

The details of the calculated electric field distribution and those of the electron, positive-ion and negative-ion
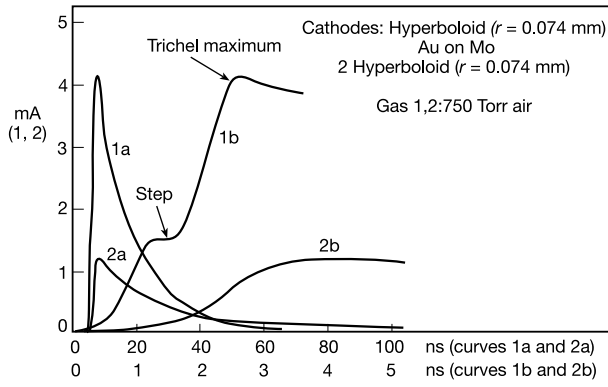
**Figure 1.** Trichel current pulses in air at atmospheric pressure (Torsethaugen and Sigmond 1973).

density distributions are presented respectively in figures 3 and 4. In air at atmospheric pressure, the principal mechanisms of the discharge responsible for the formation of Trichel pulses are similar to those found by Morrow (1985a) for a discharge in oxygen at a pressure of 6.67 kPa: the formation of a strong and positive space charge near the cathode leads to distortions of the electric field, the formation of a prominent cathode-fall region and the quenching of the current due to the swinging of the cathode-fall region in too a narrow distance to produce a significant current. In order to study those different phases, we have to present first the temporal evolution of the densities of the electrons released from the cathode (figure 5).

### 3.1. The current-multiplication phase ($t = 0$–4 ns)

At the beginning of this phase, the electric field is higher than $E^*$ at all the positions from $x = 0$ to $x = 0.2$ mm (figure 3). $E^*$ is the electric field at which the ionization coefficient equals the attachment coefficient. In air at atmospheric pressure, $E^* \simeq 30$ kV cm$^{-1}$. Consequently, the electron multiplication is the dominant process. During the first nanosecond, this electron multiplication is due to the Poisson field whereas from $t \simeq 1$ ns to $t \simeq 3$ ns the electron drift from the cathode towards the anode leads to the formation of a positive space charge (figure 3). Thus, the effects of the growth of space charge progressively become significant: the field near the cathode is enhanced whereas it is reduced between the space charge and the anode ($10^{-2} < x < 2 \times 10^{-1}$ mm). In this last region, a plasma develops, that is to say a quasi-neutral region where the electric field from its centre is low. Between the plasma and the cathode, a cathode-fall region is formed and all particle densities increase during this phase. The density of electrons released by the field effect reaches its maximum value at the end of this sequence (figure 5).

### 3.2. The current-decay phase

During this phase ($4 < t < 80$ ns), the current is progressively reduced towards zero. Two different sequences can be distinguished.
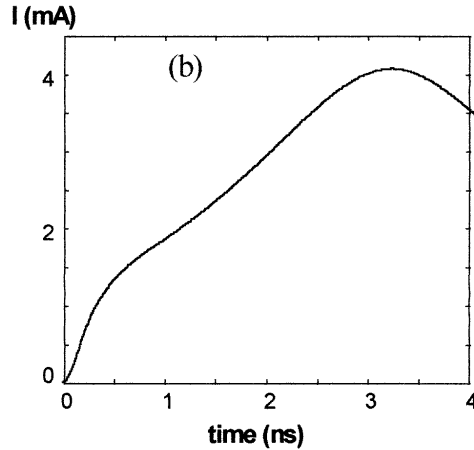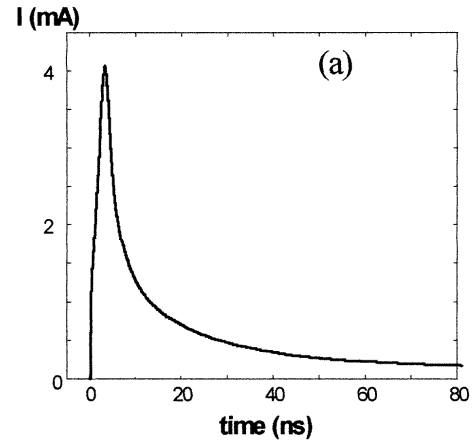


**Figure 2.** (a) The computed current versus time. (b) Details of the impulse rise time: $d = 16$ mm, $R = 0.074$ mm, $U = -4.25$ kV, $\Phi = 4.5$ eV, $\beta = 120$ and $r = 0.5$ mm.

(i) 4 ns $< t < 14$ ns $\Rightarrow |E(0, t)| \searrow$. The slow drift of the positive ions towards the cathode leads to the absorption of those ions, hence the electric field between the cathode and the plasma decreases. The electron and the positive-ion densities continue to rise until $t \simeq 6$ ns. Consequently, the density of secondary electrons, released by ions, reaches its maximum value at this time. Afterwards, the region of maximum ionization activity becomes too narrow to sustain the discharge and $E < E^*$ at all positions between the plasma and the anode. The electron and the positive-ion densities decrease gradually and electron attachment becomes the dominant process.
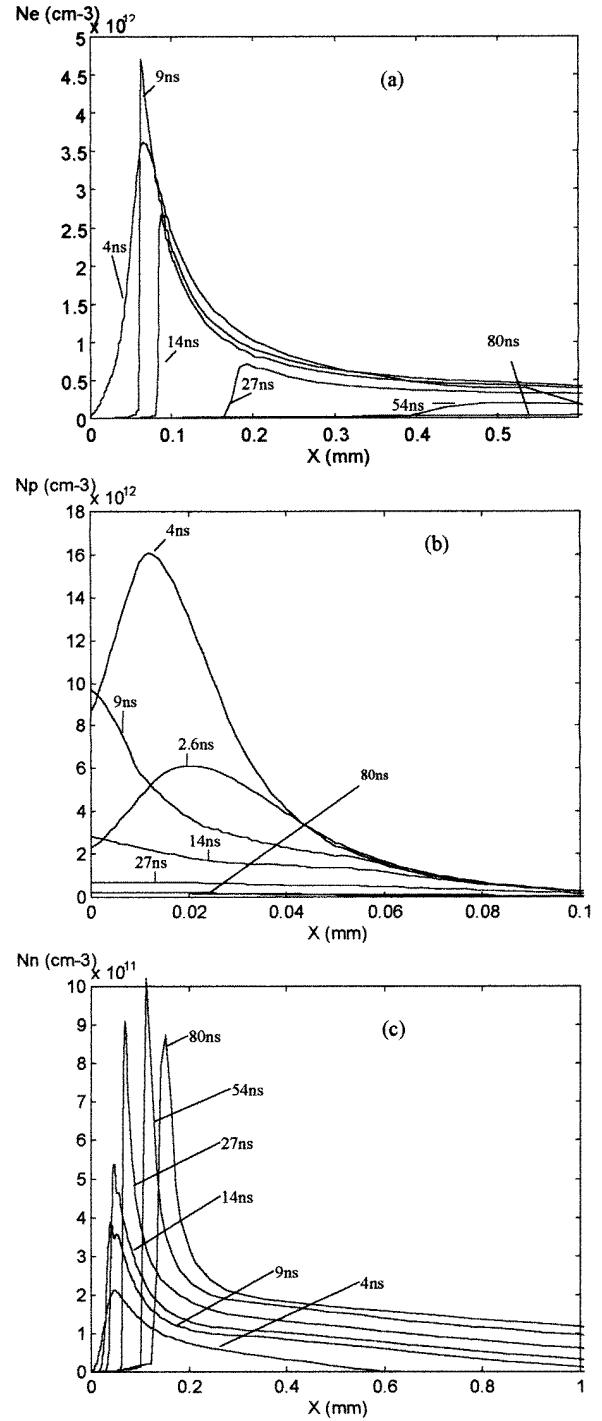
(ii) 14 ns $< t < 80$ ns $\Rightarrow |E(0, t)| \nearrow$. The three-body attachment converts electrons into negative ions. The number of those ions increases, until $N_{nmax} > N_{emax}$ at $t \simeq 27$ ns: the 'negative-ion domination phase' begins (Morrow 1985a). The electric field is controlled by the space charge of the negative ions. The slow drift of those ions towards the anode leads to a progressive increase of the electric field on the cathode. In fact, the electric field tends towards its geometrical component. The current impulse decays towards zero until the negative ions reach the anode. The main component of the electric field in the gap becomes again the geometrical component.
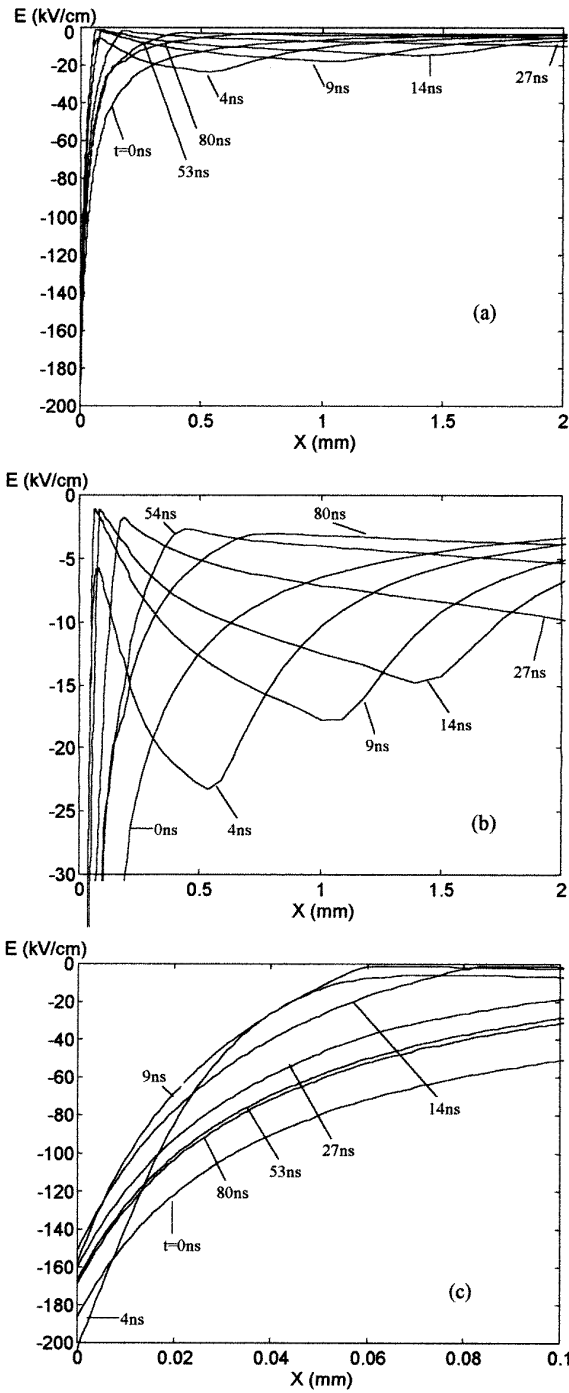
**Figure 3.** The electric field versus position at various times: (a) the field distribution from $x = 0$ to $x = 2$ mm, (b) the field distribution from $x = 0$ to $x = 2$ mm and (c) the field distribution from $x = 0$ to $x = 0.1$ mm.



**Figure 4.** Distributions of electron (a), positive-ion (b) and negative-ion (c) densities versus position at various times.

### 3.3. The step on the leading edge

The step on the leading edge of the Trichel pulse at low pressure has been explained by Morrow (1985b) in terms of two independent secondary electron emission processes: photo-ionization and positive-ion impacts. Their contribution to the current is delayed in time, producing two different peaks. In order to validate this hypothesis at high pressure (atmospheric pressure), we artificially set the secondary emission coefficient $\gamma$ to zero. The results are presented in figure 6.

The two current pulses are strictly similar. Therefore, the step on the leading edge, at high pressure, cannot be explained in terms of positive-ion impact.
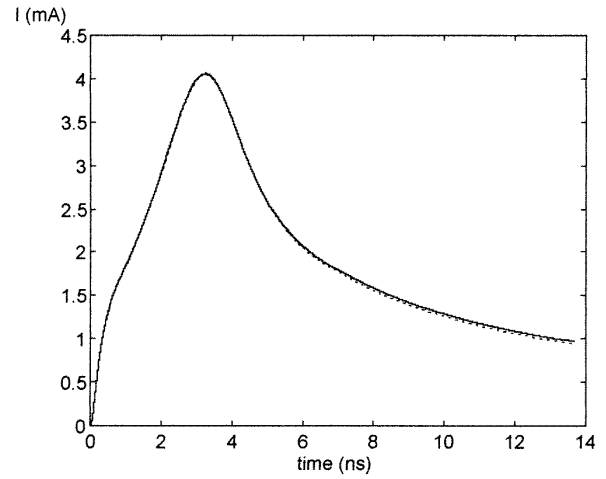
To clarify the origin of the step at high pressure, we must examine the temporal evolution of the number of
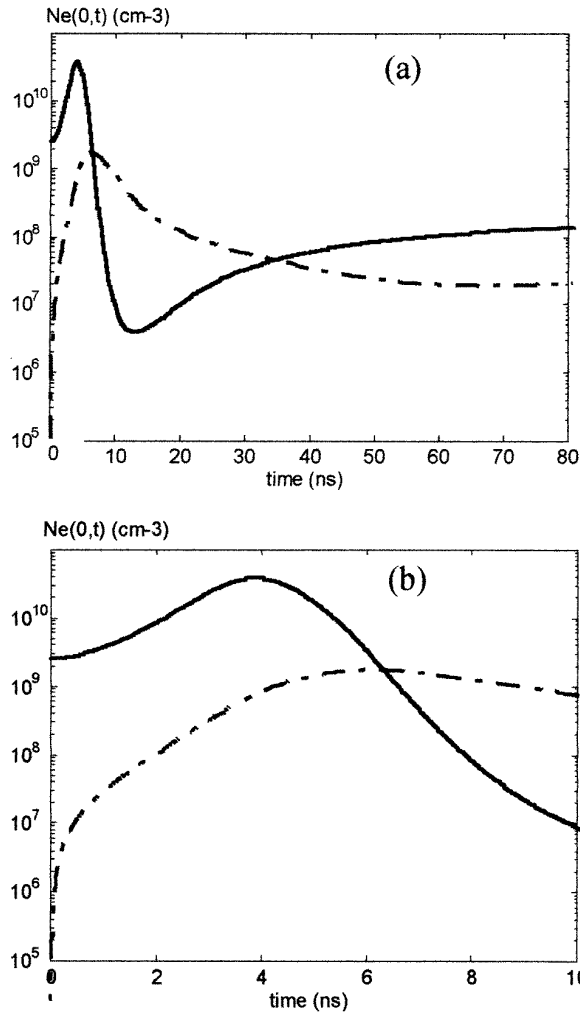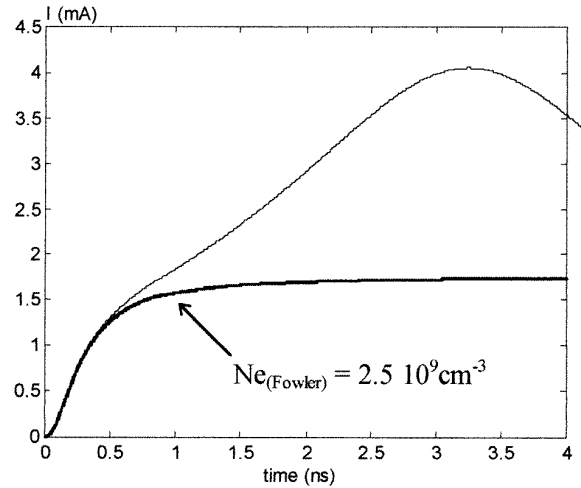
Figure 5. (a) The density of electrons released at the cathode versus time (from $t = 0$ to $t = 80$ ns). (b) The density of electrons released at the cathode versus time (from $t = 0$ to $t = 10$ ns). (———), Field-effect emission and (— · —), ion secondary electrons.



Figure 6. The computed current versus time: (———), $\gamma = 10^{-2}$; and ($\cdots\cdots$), $\gamma = 0$.



Figure 7. A comparison between the computed current pulse presented in figure 2 and the current pulse with $N_{e(Fowler)}$ artificially set to $2.5 \times 10^9$ cm$^{-3}$.

electrons released at the cathode by field-effect emission (figure 5). We have seen that, from $t = 0$ to $t \simeq 1$ ns, the effect of the space charge is negligible and the growth of current is due to the Laplace field only. Afterwards, the space-charge effects start to increase the electric field near the cathode and the number of electrons released by the field effect noticeably increases. At the same time the current is enhanced as well. Consequently, the step on the leading edge, at high pressure, could be explained in terms of cathode-sheath formation leading to a large increase in the number of electrons released at the cathode by field emission (figure 5).

This hypothesis is verified in figure 7. When the electron density released from the cathode by the field effect was artificially set to a constant value corresponding to its initial value of $2.5 \times 10^9$ cm$^{-3}$ (figure 7(b)), the peak of the current pulse was 1.5 mA and the rise time was about 1 ns (figure 7(a)). Those values characterize the step on the leading edge of the Trichel pulse.

## 4. Discussion

All the results presented have been obtained by using three characteristic parameters of the discharge and the field emission: the discharge channel radius $r$, the workfunction $\Phi$ of the cathode material and the electric field magnification factor $\beta^*$. Under the assumption that the workfunction remains constant, $\Phi$ is determined by using the mean value of the workfunctions of molybdenum and gold workfunction (figure 1), that is to say $\Phi = 4.5$ eV. The discharge channel was considered to be a cylinder of 0.5 mm radius and the field magnification factor was set to 120. The validity of those two last values will now be discussed.

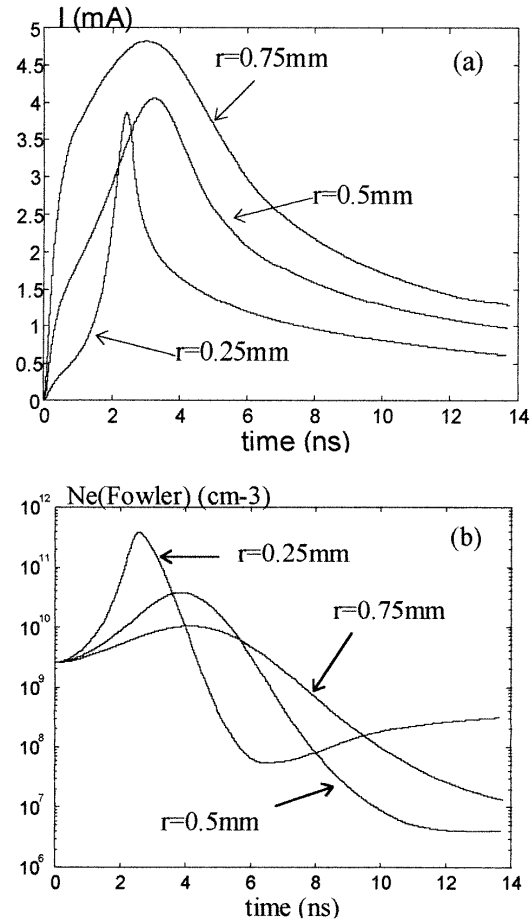### 4.1. The field magnification factor $\beta^*$

We have no physical interpretation to explain the theoretical value of 120 used in the calculation. Nevertheless, this
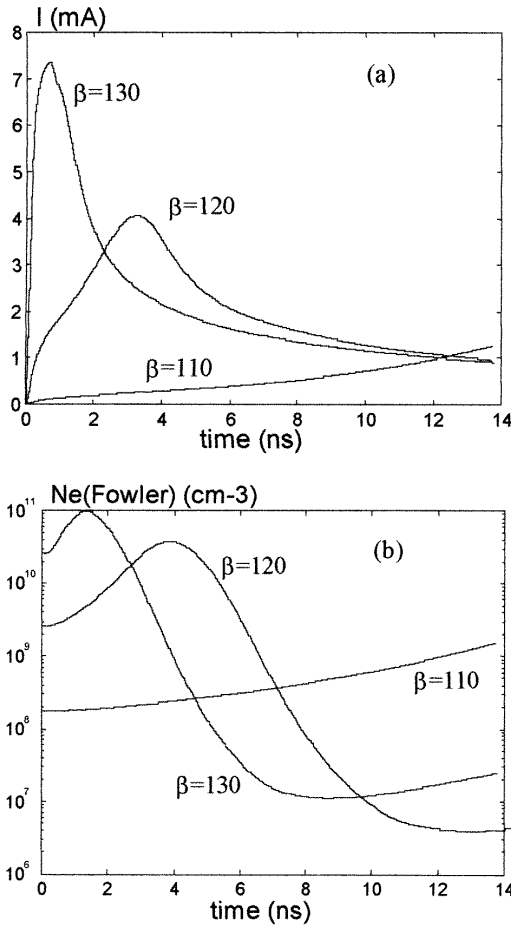
**Figure 8.** Computed current waveforms (a) for various values of the field magnification factor $\beta^*$ and the associated temporal evolution (b) of the electron density released by the field effect. $d$ = 16 mm, $R$ = 0.074 mm, $U$ = −4.25 kV, $\Phi$ = 4.5 eV and $r$ = 0.5 mm.



**Figure 9.** Computed current waveforms (a) for various values of the discharge channel radius $r$ and the associated temporal evolution (b) of the electron density released by the field effect. $d$ = 16 mm, $R$ = 0.074 mm, $U$ = −4.25 kV, $\Phi$ = 4.5 eV and $\beta$ = 120.

value can be compared to those experimentally measured by several authors: Rohrbach (1971) showed that the electric field at the top of cathode protrusions can be easily multiplied in the range from 10–1000. More exactly, Williams and Williams (1972) determined the values of the field magnification factor for electrodes with different surface finish. Their results showed that, for polished electrodes, the value of $\beta^*$ is in the range 80–130. These results are in good accordance with the value of $\beta^* = 120$ used for our calculation.

Figure 8(a) shows three computed current waveforms obtained for various values of $\beta^*$. When $\beta^* = 130$, the electron density released by the field effect is more important and the cathode-fall region develops earlier in time (figure 8(b)). Consequently, the current peak value is about 7 mA and its time to peak is shorter than 1 ns. When $\beta^* = 110$, the electron density released by the field effect increases very slowly until $t = 14$ ns: the current peak still has not been reached at this time. Consequently, these three calculations obviously show that the theoretical result, which is in good agreement with the experimental one, is obtained for $\beta^* = 120$.

### 4.2. The channel radius of the discharge $r$

The channel radius $r$ of the discharge is an essential model input parameter. For the calculation, the discharge is considered to be a cylinder of 0.5 mm radius centred on the axis of symmetry of the system. This value is of the same order as the one experimentally determined by Loeb (1965) in air at atmospheric pressure for a 0.19 mm radius point.

Three computed current waveforms, obtained for various values of $r$, are presented in figure 9(a). For high values of the channel radius, the time to peak of the current is longer and the peak value is higher. Moreover, the pulse width depends on the radius value. In order to explain these results, we have to refer to the electric field relationship (3): the electric field amplitude is inversely proportional to the value of ($r$). Figure 9(b) shows the temporal evolution of the electron density released by the field effect. Owing to the high value of the space-charge electric field near the cathode, the number of secondary electrons is higher for $r = 0.25$ mm. As a result, the development of the cathodic fall region and the quenching of the current occur earlier in this case.

The channel radius plays a crucial role in the development of the discharge. The amplitude of the electric

field directly depends on the radius value. Consequently the elementary processes involved in the propagation of the discharge, which are representable as functions of the reduced electric field, mainly depend on the channel radius.

Nevertheless, in all 1D numerical models this parameter is defined without physical interpretation but only in accordance with experimental results. In this study, the value of $r = 0.5$ mm is in good agreement with the experimental one measured by Loeb (1965) and allows one to calculate a current pulse in accordance with the one measured by Torsthaugen and Sigmond (1973).

## 5. Conclusion

We have presented a numerical simulation of a Trichel pulse in air at atmospheric pressure in good agreement with the experimental results. For the first time, this simulation explains the fast rise time of the current pulse (at high pressure) in terms of field-effect emission. We have demonstrated that the secondary emission at high pressure plays a negligible role in comparison with the field-effect emission. The step on the leading edge of the Trichel pulse can be explained in terms of the large and sudden increase in the number of electrons released by the field effect due to the formation of a cathode sheath.

Moreover, this simulation allows one to take the cathode material and its surface state into account. The influences of the field magnificator factor and the discharge channel radius on the Trichel pulse are pointed out.

## Acknowledgments

## References

Bayle P 1975 *Thèse* Université de Toulouse
Borris J P and Book D L 1976 *J. Comput. Phys.* **20** 397–431
Boutteau M 1967 Internal note of EDF number 022/21
Cernak M and Hosokawa A T 1991 *Phys. Rev.* A **43** 1107–9
——1992 *Aust. J. Phys.* **45** 193–219
Davies A J and Evans C J 1967 *Proc. IEE.* **114** 1547–50
Fowler R H and Nordheim L 1928 *Proc. R. Soc.* A **119** 173
Laurence T, Mickey P and Dressler J 1968 *J. Chem. Phys.* **48** 1989
Lama W L and Gallo C F 1974 *J. Appl. Phys.* **45**
Loeb L B 1965 *Electrical Coronas: Their Basic Physical Mechanisms* (Berkeley, CA: University of California Press)
Morrow R 1985a *Phys. Rev.* A **32** 1799–809
——1985b *Phys. Rev.* A **35** 3821–4
——1987 *Phys. Rev.* A **35** 1778–85
Morrow R and Cram L E 1983 *Computational Techniques and Applications Conf., (Sydney)* ed J Noye and C H J Fletcher (Amsterdam: North-Holland) pp 719–30
——1985 *J. Comput. Phys.* **57** 129–36
Reess T, Ortega P, Gibert A, Domens P and Pignolet P 1995a *J. Phys. D: Appl. Phys.* **28** 2306–13
Reess T, Ortega P, Gibert A, Paillol J, Domens P and Pignolet P 1995b *Proc. 11th Int. Conf. on Gas Discharges, (Tokyo)* vol 1 (Japan: IEEE) p 120
Reess T, Paillol J, Gibert A and Domens P 1997 *2nd European Conf. on Numerical Methods in Electromagnetism, (Lyon)* (Lyon: L'Ecole Centrale de Lyon) p 234
Rohrbach F 1971 CERN 71-5, Division des chambres à traces (TC-L)
Sato N 1980 *J. Phys. D: Appl. Phys.* **13** L3
Steinle P and Morrow R 1989 *J. Comput. Phys.* **80** 61–71
Torsethaugen K and Sigmond R S 1973 *Proc. 11th Int. Conf. on Phenomena in Ionized Gases, Prague*
Trichel G W 1938 *Phys. Rev.* **54** 1078
Wang M C and Kunhart E E 1990 *Phys. Rev.* A **42** 2366–73
Williams D W and Williams W T 1972 *J. Phys. D: Appl. Phys.* **5** 1845–54
Zalesak S T 1979 *J. Comput. Phys.* **31** 355